A simple numerical experiment on the dust temperature bias for Lyman break galaxies at $z \gtrsim 5$

Yung Ying Chen,[1]★ Hiroyuki Hirashita ®,[1]★ Wei-Hao Wang[1] and Naomasa Nakai[2]

[1]*Institute of Astronomy and Astrophysics, Academia Sinica, Astronomy-Mathematics Building, No. 1, Section 4, Roosevelt Road, Taipei 10617, Taiwan*
[2]*School of Science and Technology, Kwansei Gakuin University, 2-1 Gakuen, Sanda, Hyogo 669-1337, Japan*

ABSTRACT

Some studies suggest that the dust temperatures (T_d) in high-redshift ($z \gtrsim 5$) Lyman break galaxies (LBGs) are high. However, possible observational bias in T_d is yet to be understood. Thus, we perform a simple test using random realizations of LBGs with various stellar masses, dust temperatures, and dust-to-stellar mass ratios and examine how the sample detected by Atacama Large Millimetre/submillimetre Array (ALMA) is biased in terms of T_d. We show that ALMA tends to miss high-T_d objects even at total dust luminosity $L_{IR} > 10^{11}$ L$_\odot$. LBGs are, however, basically selected by the stellar UV luminosity. The dust-temperature bias in a UV-selected sample is complicated because of the competing effects between high T_d and low dust abundance. For ALMA Band 6, there is no tendency of high-T_d LBGs being more easily detected in our experiment. Thus, we suggest that the observed trend of high T_d in $z \gtrsim 5$ LBGs is real. We also propose that the 450 μm band is useful in further clarifying the dust temperatures. To overcome the current shallowness of 450 μm observations, we examine a future Antarctic 30-m class telescope with a suitable atmospheric condition for wavelengths $\lesssim$450 μm, where the detection is not confusion-limited. We find that, with this telescope, an L_{IR}-selected sample with $\log(L_{IR}/L_\odot) > 11$ is constructed for $z \gtrsim 5$, and detection in the intermediate-$M_\star$ (stellar mass) range [$9 < \log(M_\star/M_\odot) < 9.5$] is much improved, especially at high T_d.

Key words: dust, extinction – galaxies: evolution – galaxies: high-redshift – galaxies: statistics – infrared: galaxies – submillimetre: galaxies.

1 INTRODUCTION

Dust grains are widespread in the interstellar medium (ISM) that is the ingredient of star formation. Dust also absorbs and scatters the radiation from formed stars in the ISM, and reprocesses it in the infrared (IR)–submillimetre (submm; e.g. Buat & Xu 1996; Calzetti et al. 2000). These radiative processes of dust are important in the following two aspects. First, to estimate the star formation rate in a galaxy using the stellar light, correction for dust extinction is crucial (e.g. Steidel et al. 1999; Inoue, Hirashita & Kamaya 2000). Secondly, dust largely affects the spectral energy distributions (SEDs) of galaxies (e.g. Silva et al. 1998; Takagi, Vansevicius & Arimoto 2003; Takeuchi et al. 2005). Since SEDs are used to extract various information (stellar mass, age, etc.; e.g. da Cunha, Charlot & Elbaz 2008; Boquien et al. 2019), it is fundamentally important to appropriately consider dust extinction and emission. Dust also affects the physical and chemical states of the ISM. Dust surfaces provide reaction sites for forming some molecular species (e.g. Chen et al. 2018), especially molecular hydrogen (e.g. Gould & Salpeter 1963; Cazaux & Tielens 2004), leading to the formation of molecule-rich environments in galaxies (e.g. Hirashita & Ferrara 2002; Yamasawa et al. 2011). In the star formation process, dust cooling induces fragmentation of molecular clouds and shapes the stellar initial mass

function (e.g. Whitworth, Boffin & Francis 1998; Schneider et al. 2006; Larson 2005; Omukai et al. 2005). Because of the above important roles of dust, it is crucial to clarify the origin and evolution of dust in the Universe.

Observing the high-redshift Universe is useful to know how galaxies are enriched with dust in the early phase of their evolution. The current frontier of dust observation lies at $z \gtrsim 5$ (e.g. Capak et al. 2015; Casey et al. 2018; Burgarella et al. 2020; Zavala et al. 2021), where z is the redshift; thus, in this paper, high-redshift indicates $z \gtrsim 5$. With the Atacama Large Millimetre/submillimetre Array (ALMA), dust emission from high-redshift galaxies has become accessible (e.g. Dayal & Ferrara 2018). In particular, dust emission has been detected for a 'typical' population of high-redshift galaxies, Lyman break galaxies (LBGs), even at $z > 7$ (Watson et al. 2015; Laporte et al. 2017; Hashimoto et al. 2019; Tamura et al. 2019; Schouws et al. 2021). However, most of the LBGs at such high redshift remain undetected even with ALMA (e.g. Riechers et al. 2014; Bouwens et al. 2016; Fudamoto et al. 2020).

The dominant source of dust at high redshift is still being debated (e.g. Leśniewska & Michałowski 2019). Dust grains condense in stellar ejecta: supernovae (SNe) are expected to be the first dust sources in the Universe because their progenitors have short lifetimes (e.g. Todini & Ferrara 2001; Nozawa et al. 2003). However, a part of the dust formed in SNe could be destroyed in the shocked region before being injected into the ISM (e.g. Bianchi & Schneider 2007; Nozawa et al. 2007). Thus, it is not obvious if SNe produce a sufficient amount of dust in the early stage of galaxy evolution.

To 'supplement' the dust abundance, it has been suggested that dust growth by the accretion of gas-phase metals in the dense ISM dominates the increase of dust mass in some high-redshift galaxies (e.g. Mancini et al. 2015; Wang, Hirashita & Hou 2017a; Liu & Hirashita 2019).

To observationally reveal the dust sources at high redshift, it is important to correctly estimate the dust mass. The estimate of dust temperature is particularly important in deriving the dust mass in galaxies. Even if we fix the dust mass absorption coefficient (which is generally uncertain), the uncertainty (or the lack of knowledge) in the dust temperature highly nonlinearly affects the dust mass estimate. Some studies estimated the dust temperatures in high-redshift LBGs basically from rest-frame far-IR (FIR) multiwavelength data. Knudsen et al. (2017), using the detection of a LBG at $z = 7.5$ (A1689zD1; first detected with ALMA by Watson et al. 2015) in ALMA Band 6 and Band 7, obtained a dust temperature of 35–45 K, which is higher than the typical dust temperatures in the local spiral galaxies ($\sim$20–25 K; e.g. Draine et al. 2007; Skibba et al. 2011). Inoue et al. (2020) and Bakx et al. (2021) further added a detection in Band 8 and 9, respectively, and confirmed the high dust temperature. Burgarella et al. (2020) compiled detected LBGs at various $z(>5)$ to trace SEDs at different restframe FIR wavelengths. In this way, they derived typical dust temperatures of 40–70 K, higher than those in local spiral galaxies. Bakx et al. (2020) obtained a dust temperature of >80 K for a LBG at $z = 8.31$. Faisst et al. (2020) observed four LBGs at $z \sim 5.5$ and derived high dust temperatures of 30–43 K. These high dust temperatures at high redshift imply that adopting a typical dust temperature in nearby spiral galaxies systematically overestimates the dust mass at high redshift.

The dust temperatures also give a clue to the physical condition in high-redshift galaxies. A trend of higher dust temperatures at higher redshift is also seen at $z \lesssim 4$ (Béthermin et al. 2015; Schreiber et al. 2018), and could be related to higher star formation efficiencies (Magnelli et al. 2014). There are other possible theoretical reasons for high dust temperatures in high-z LBGs. For example, if high-redshift galaxies host compact star-forming regions or high surface densities of star formation rate, the dust temperature is expected to be higher (Ferrara et al. 2017; Ma et al. 2019; Sommovigo et al. 2020).

The above understanding of the dust temperatures in high-redshift galaxies is far from complete and is perhaps biased. It is difficult to obtain fluxes from high-redshift LBGs in multiple ALMA bands precisely enough to determine a well-constrained dust temperature. The detectability is also affected by the dust temperature; in particular, if the dust temperature is high as indicated above, ALMA submm–millimetre bands may miss the peak of dust emission located at shoter wavelengths (e.g. Hirashita, Burgarella & Bouwens 2017). If the dust temperature is low, the emission is inefficient so that the dust is faint in the ALMA bands. These effects of dust temperature could hamper our unbiased understanding of dust evolution in high-redshift galaxies.

In principle, the dust temperature bias can be addressed if we theoretically predict the dust temperature distribution of high-redshift LBGs. However, predicting the statistical properties of dust temperature is not easy because of the following issues. The first problem is low spatial resolution. Although some cosmological simulations (e.g. Springel & Hernquist 2003) successfully included dust evolution (e.g. McKinnon et al. 2017; Aoyama et al. 2018; Hou et al. 2019; Graziani et al. 2020) and predicted dust temperatures (e.g. Aoyama et al. 2019), simulations on galactic or larger scales generally have a low spatial resolution. Because of this limitation, an intense radiation field from compact star-forming regions, which

could be important for explaining the high dust temperatures at high redshift, is difficult to investigate. Spatially unresolved treatments such as semi-analytic models (Valiante et al. 2011; de Bennassuti et al. 2014; Popping, Somerville & Galametz 2017; Ginolfi et al. 2018) and post-processing models (Mancini et al. 2016; Huang et al. 2021) have difficulty in predicting the dust temperature. The second is a small sample size. Some zoom-in simulations succeeded in investigating the details of dust distribution (Yajima et al. 2015; McKinnon, Torrey & Vogelsberger 2016; Gjergo et al. 2018; Granato et al. 2021) and dust temperatures (e.g. Liang et al. 2019; Ma et al. 2019; Di Mascia et al. 2021), but the conclusion may rely on the zoomed particular objects.

In this paper, we aim at clarifying if there is any bias for the dust temperature in a sample of high-redshift ($z \gtrsim 5$) LBGs observed by ALMA. Since theoretical methods (i.e. simulations and semi-analytic models) have limitation as mentioned above, we take a different, simple approach based on random realizations of LBGs; that is, we construct a virtual big sample of LBGs that enables us to examine the statistical properties of the dust temperatures. The realizations are based on random sampling of some fundamental observational quantities whose ranges are constrained empirically by observed LBGs at $z \gtrsim 5$. In this way, a big sample is easy to generate. Based on this virtual sample, we examine how the detected LBGs are biased in terms of the dust temperature. The bias clarified through this approach will serve to judge if the observed high dust temperatures at high redshift reflect a real trend or an observational selection effect.

In addition, we investigate a possibility of improving the dust temperature estimate. Besides the often used bands at 850 and 1200 μm (Bands 7 and 6, respectively), we add 450 μm (Band 9), which is near to the SED peak of galaxies at $z \gtrsim 5$ or even on Wien's side depending on the dust temperature (e.g. Bakx et al. 2021). The usefulness of the 450 μm band is demonstrated at lower redshifts ($z < 5$). Casey et al. (2013) showed that the dust temperatures of 850 and 450 μm samples in their survey using the SCUBA-2 instrument on the James Clerk Maxwell Telescope (JCMT) are different: The 450 μm band tends to detect galaxies with higher dust temperatures. Recently, the SCUBA-2 Ultra Deep Imaging East Asian Observatory Survey (STUDIES) has been conducted at 450 μm, starting to detect galaxies at the knee of the IR luminosity function up to $z \sim 3$ (Wang et al. 2017b). Optical counterpart identifications and multiwavelength SED fitting were successfully performed up to $z \sim 4$ (Lim et al. 2020; Dudzevičiūtė et al. 2021). It is highly probable that the 450 μm band is also useful at $z \gtrsim 5$; thus, we discuss the detectability at 450 μm in this paper.

As we will show later, the worse sensitivity at 450μm is worse than at 850 and 1200 μm limits the dust temperature studies at $z \gtrsim 5$. For a further improvement of 450 μm observations, we consider a future Antarctic large single-dish telescope as a representative plan, and discuss if such a future telescope contributes to a further understanding of the dust temperatures in high-redshift LBGs. Observations at such a short submm wavelength, or at a nearly tera-hertz (THz) frequency, require a low water vapour content in the atmosphere, and are best carried out from Antarctic sites and Greenland (e.g. Hirashita et al. 2016; Matsushita et al. 2017). A similar scientific goal could also be achieved by future >30-m-class submm telescopes, such as the Atacama Large-Aperture Submmillimetre/millimetre Telescope (Klaassen et al. 2020) and the Large Submillimetre Telescope (Kawabe et al. 2016).

This paper is organized as follows. We explain the method for generating a LBG sample in Section 2. We show the results in Section 3. We discuss some further issues, especially possible improvement

using a future telescope in Section 4. Section 5 concludes this paper. We adopt the following cosmological parameters: cosmological constant parameter $\Omega_\Lambda = 0.7$, total matter density parameter $\Omega_M = 0.3$, and Hubble constant $H_0 = 70$ km s^{-1} Mpc^{-1}.

2 MODEL

We use a simple method based on random sampling of the relevant parameter ranges for basic quantities that characterize the dust emission in high-redshift ($z \geq 5$) LBGs. We focus on LBGs as a representative population for high-redshift galaxies, and exclude extreme populations such as submm galaxies (SMGs) and quasars. We first describe our assumptions. Next, we discuss how the basic quantities are related to the dust emission luminosity and the observed flux. Finally, for the purpose of parameter surveys, we generate random realizations of LBGs, which are virtually observed to discuss possible temperature biases in detected objects.

2.1 Assumptions

We assume that the dust emission from a LBG is characterized by stellar mass $M_\star$, dust-to-stellar mass ratio $\mathcal{D}_\star$, and dust temperature T_d. LBGs at $z \gtrsim 5$ are mostly selected by rest-frame UV flux, which is well correlated with the stellar mass (Schaerer et al. 2015; see also Section 2.2). Thus, we assume that the stellar mass is one of the most fundamental quantities. Indeed, Burgarella et al. (2020) normalized both star formation rate and dust mass by the stellar mass, and found a meaningful relation between these two quantities. This supports our idea of using $M_\star$ for the overall scaling factor. Moreover, we also expect that the dust enrichment, strongly related to metal enrichment, proceeds along with the buildup of stellar mass (or the metal enrichment associated with star formation; e.g. Tinsley 1980). To obtain the dust mass, M_d, we use the dust-to-stellar mass ratio ($\mathcal{D}_\star$; referred to as the specific dust mass in Burgarella et al. 2020) for the second parameter. Using this quantity, the dust mass M_d is given by $M_d = \mathcal{D}_\star M_\star$. Finally, with a given dust mass (and dust mass absorption coefficient), the total dust luminosity is determined by the dust temperature. Thus, we use T_d for the third parameter. Since T_d is used to estimate the dust emission luminosity, T_d is interpreted as luminosity-weighted dust temperature (e.g. Liang et al. 2019).

As mentioned above, we assume that the dust heating sources (i.e. stars) are mostly traced by rest-frame UV observations. This reflects the fact that high-redshift LBGs are first sampled by their rest-frame UV emission. Because of this selection, we do not treat highly embedded star formation activities as seen in extreme starbursts (such as SMGs). This assumption is equivalent to the hypothesis that the total IR luminosity L_{IR} is not much higher than the UV luminosity L_{UV}. The ratio L_{IR}/L_{UV} is referred to as the IR excess (IRX). Indeed, IRX $\lesssim 10$ for high-z LBGs (Bouwens et al. 2016; Burgarella et al. 2020). (We discuss the value of IRX further in Section 2.3.) Thus, we adopt the set of parameters ($M_\star$, $\mathcal{D}_\star$, T_d) under the constraint that IRX does not exceed a certain value ($\sim$1–10).

At high redshift, the effect of the CMB heating on the dust temperature may not be negligible. Thus, T_d is not totally free because it cannot drop below the CMB temperature. To include this effect, we first input the 'virtual' dust temperature, T_d^0, which would be realized if there is no heating from the CMB, and then correct it for the CMB heating. We treat T_d^0 as a free input parameter. The dust temperature after correcting for the CMB effect is obtained by (da Cunha et al. 2013)

$$T_d = \left\{ \left(T_d^0\right)^{4+\beta_{IR}} + \left(T_{CMB}^0\right)^{4+\beta_{IR}} \left[(1+z)^{4+\beta_{IR}} - 1\right] \right\}^{\frac{1}{4+\beta_{IR}}}, \quad (1)$$

Table 1. Dust species.

Species	κ_{158} (cm^2 g^{-1})	β_{IR}	C_{IR} (See text)
Silicate	13.2	2	3.5×10^{-6}
Graphite	20.9	2	5.6×10^{-6}
AC	28.4	1.4	4.3×10^{-5}

The values of κ_{158} and β_{IR} are taken from Hirashita et al. (2014).

where β_{IR} is the dust emissivity index (given in equation 3) and T_{CMB}^0 is the CMB temperature at $z = 0$ (2.73 K).

2.2 Calculation of the dust luminosity and flux

We assume that the dust emission follows the so-called modified blackbody spectrum with a single dust temperature. Thus, the monochromatic luminosity of the dust emission at rest-frame frequency ν (denoted as L_ν) is estimated by the following equation (e.g. Dayal, Hirashita & Ferrara 2010):

$$L_\nu = 4\pi \kappa_\nu M_d B_\nu(T_d), \quad (2)$$

where κ_ν is the mass absorption coefficient at frequency ν, and $B_\nu(T_d)$ is the Plank function at frequency ν and temperature T_d. The mass absorption coefficient is estimated by assuming a power-law form as (e.g. Hirashita et al. 2014)

$$\kappa_\nu = \kappa_{158} \left(\frac{\nu}{\nu_{158}} \right)^{\beta_{IR}}, \quad (3)$$

where κ_{158} is the value at a wavelength (λ) of 158 μm, ν_{158} is the frequency corresponding to $\lambda = 158$ μm, and β_{IR} is the dust emissivity index. The choice of the wavelength for normalization is arbitrary. For the dust species, we adopt the following often adopted materials: silicate, graphite, and amorphous carbon (AC). We adopt the values of κ_{158} and β_{IR} for each species as listed in Table 1. We use graphite unless otherwise stated, since it has an intermediate mass absorption coefficient. We discuss the other species in Section 4.1. The observed flux at frequency ν (denoted as f_ν) is estimated as (da Cunha et al. 2013)

$$f_\nu = \frac{(1+z)}{d_L^2} \kappa_{\nu(1+z)} M_d \left[B_{\nu(1+z)}(T_d) - B_{\nu(1+z)}(T_{CMB}) \right], \quad (4)$$

where $T_{CMB} = T_{CMB}^0 (1+z)$ is the CMB temperature at redshift z and d_L is the luminosity distance given by e.g. Carroll, Press & Turner (1992).

As mentioned above, we exclude highly dust-obscured objects, which cannot be selected as LBGs. This means that IRX is not extremely large. Thus, we impose a maximum IRX, IRX$_{max}$, which is a free parameter in this paper. In what follows, we explain how to calculate the IR and UV luminosities, and IRX.

The IR luminosity (denoted as L_{IR}) is evaluated by

$$L_{IR} \equiv \int_0^\infty L_\nu \, d\nu = C_{IR}(M_d/M_\odot)(T_d/K)^{\beta_{IR}+4} \, L_\odot, \quad (5)$$

where C_{IR} can be numerically evaluated by integrating equation (2) together with equation (3) for κ_ν. The obtained value of C_{IR} is given for each dust species in Table 1.

To calculate the UV luminosity (denoted as L_{UV}), we assume that L_{UV} is converted from $M_\star$ with a factor α:

$$L_{UV} = \alpha M_\star. \quad (6)$$

We take the standard value of α (denoted as α_0) from Schaerer et al. (2015; see also Wang et al. 2017a), who derived an almost linear relation between $L_{\rm UV}$ and $M_\star$ for LBGs at $z \sim 6.7$: $\alpha_0 = 15.6(\rm L_\odot/M_\odot)$ based on their value at $M_\star = 10^9 \, \rm M_\odot$. We confirm that this value of α_0 is consistent with the relation between $L_{\rm UV}$ and $M_\star$ derived from SED fitting within a factor of ~ 3 for the major part of Burgarella et al. (2020)'s sample [except for a couple of low-$M_\star$ ($<10^9 \, \rm M_\odot$) objects with $\alpha \gtrsim 100(\rm L_\odot/M_\odot)$ because of young ($\sim 10^7 \, \rm yr$) stellar ages; we separately discuss high α in Section 3.3.3]. Considering the above factor 3 variation, we give α for each object as $\alpha = 10^\delta \alpha_0$, where δ is randomly chosen from $[-0.5, 0.5]$. In reality, α depends on the dust extinction and the stellar age, but we avoid including this complication in our model in order to keep the simplicity. Thus, we take the above approach; that is, we choose α randomly for each object (by implicitly assuming that the physical parameters regulating δ vary randomly).

Using the above $L_{\rm IR}$ and $L_{\rm UV}$, we obtain IRX (noting that $\mathcal{D}_\star = M_{\rm d}/M_\star$) as

$$\rm IRX = C_{\rm IR}\mathcal{D}_\star T_{\rm d}^{\beta_{\rm IR}+4}/\alpha. \tag{7}$$

If IRX is larger than a certain threshold $\rm IRX_{\rm max}$, we regard this object as a highly obscured galaxy, and remove it from the sample. We adopt $\rm IRX_{\rm max} \lesssim 10$ based on actually observed values (Bouwens et al. 2016; Burgarella et al. 2020) and further discuss it in Section 3.1.

2.3 Parameter setup

In our model, we give $(M_\star, \mathcal{D}_\star, T_{\rm d}^0)$ for each galaxy. Since the statistical distribution of these quantities are poorly known, we select the values of these quantities randomly in the ranges by referring to actually observed or theoretically expected for high-redshift LBGs. For the stellar mass and dust-to-stellar mass ratio, we refer to Burgarella et al. (2020) and Nanni et al. (2020) for the ranges and adopt $\log (M_\star/\rm M_\odot) = 8.0\text{--}10.0$ and $\log \mathcal{D}_\star = (-4)\text{--}(-1.5)$. Pozzi et al. (2021) derived $M_{\rm d} \lesssim 10^{7.5} \, \rm M_\odot$ for $M_\star \sim 10^{9.2}\text{--}10^{9.9}$ $\rm M_\odot$ [converted from the observed UV luminosities using equation 6 with $\alpha = 15.6 \, (\rm L_\odot/M_\odot)$] at $z \sim 5$, indicating $\log \mathcal{D}_\star \lesssim (-1.7)\text{--}(-2.4)$. This is consistent with the adopted range of $\mathcal{D}_\star$. For the stellar mass range, there are galaxies with $M_\star > 10^{10} \, \rm M_\odot$ at high redshift, but they usually belong to populations different from LBGs, such as SMGs (e.g. Michałowski et al. 2017). We choose a logarithmic values for $M_\star$ and $\mathcal{D}_\star$ randomly from the above ranges.

For the dust temperature, since our purpose is to clarify the dust temperature bias, we slightly extend the range from 40 to 70 K, which is derived by Burgarella et al. (2020). This temperature range covers the dust temperatures estimated with various methods (Faisst et al. 2017; Hashimoto et al. 2019; Inoue et al. 2020; Bakx et al. 2021; Sommovigo et al. 2021). We extend the range towards both lower and higher temperatures and adopt $T_{\rm d}^0 = 20\text{--}85$ K. Burgarella et al. (2020) showed in their fig. 1 that some LBGs may be consistent with $T_{\rm d} = 85$ K if we take the uncertainties into account. Bakx et al. (2020) obtained a constraint for the dust temperature of an LBG at $z = 8.3$ as >80 K, which justifies the above extension to a high dust temperature. A SMG AzTEC-3 has a dust temperature of 92 K (Riechers et al. 2020). Although we exclude SMGs from our modelling, this object demonstrates a possibility that some high-redshift galaxies may have an extremely high dust temperature. Numerical simulations, on the other hand, show moderate dust temperatures lower than 40 K (Ma et al. 2019; Liang et al. 2019). Because we do not know the real dust temperature range, we extend it down to 20 K, which is a typical dust temperature in nearby star-forming galaxies (e.g. Draine et al. 2007). The lowest dust temperature is not very important since the CMB

limits the lowest temperatures achieved at high redshift (equation 1). However, we should note again that the wide temperature range is adopted for the purpose of examining possible temperature biases. We leave the determination of the correct temperature range for a future study because we need a larger observational sample with a uniform sensitivity and a further development of a dedicated statistical tool.

For the redshift, we examine $z = 5$, 7, and 10. Including $z = 10$ is useful to discuss the possibility of expanding the redshift frontier of the current observations. The number of generated objects is adjusted to obtain statistically meaningful results as described below.

2.4 Selection of LBGs detectable with ALMA

Our main purpose is to examine the dust temperature bias for the detected objects. For a representative sensitivity, we consider ALMA observations. Although our quantitative conclusions are only valid for ALMA, the same biases are qualitatively expected for other (including future) submm telescopes. As mentioned in the Introduction, we use Bands 6, 7, and 9 of ALMA in this study. Band 8 ($\sim$750 μm) is also used for the studies of high-redshift galaxies (e.g. Faisst et al. 2020; Inoue et al. 2020), but Band 8 gives similar results to Band 7 for the diagrams we show below. Thus, we omit Band 8 for the conciseness of presentation. With the ALMA sensitivity calculator,[1] the 3σ detection limits with 1 h integration time at 450, 850, and 1200 μm (Bands 9, 7, and 6, respectively) are 0.81, 0.088, and 0.063 mJy, respectively. We also examine a deeper observation with 5 h integration with 3σ limits of 0.36, 0.039, and 0.028 mJy at 450, 850, and 1200 μm, respectively. If we aim at 5σ detection with the same sensitivities, we require an integration time roughly three times longer.

3 RESULT

3.1 Effect of the criterion on IRX

Before showing our results, we examine the effect of imposing the condition $\rm IRX < IRX_{\rm max}$ (Section 2.2). We generate 3 000 LBGs. In Fig. 1, we show how the criterion for IRX affects the sample properties in the parameter space. The 3D parameter space is projected on to the $T_{\rm d}\text{--}\mathcal{D}_\star$ and $T_{\rm d}\text{--}M_\star$ planes. We show the data at $z = 7$; however, except for the lowest dust temperature determined by the CMB temperature, this figure does not depend on the redshift.

We observe that the IRX value mainly constraints the higher end of the dust temperature and that the highest dust temperature decreases if we impose a severer upper limit on IRX (i.e. smaller $\rm IRX_{\rm max}$). The upper bound of dust temperature strongly depends on $\mathcal{D}_\star$. For a higher dust abundance ($\mathcal{D}_\star$), a high IR luminosity is more easily achieved, so that the dust temperature is strongly constrained from the upper limit of IRX. From equation (7), the boundary is described by $\mathcal{D}_\star T_{\rm d}^{\beta_{\rm IR}+4} = \alpha \rm IRX_{\rm max}/C_{\rm IR}$. We regard the $\mathcal{D}_\star$-dependent upper bound for $T_{\rm d}$ as a physically reasonable constraint, since, with a limited amount of dust-heating sources (stars), a large amount of dust cannot be equally heated to a high temperature. In other words, $\mathcal{D}_\star$ and $T_{\rm d}$ are not completely independent. Therefore, we do not use $\mathcal{D}_\star$ explicitly as an independent variable in statistical discussions in Section 4. In the $T_{\rm d}\text{--}M_\star$ diagram, there is no clear temperatures trend along the $M_\star$ axis. The objects occupy both high and low dust temperature regions at any $M_\star$.
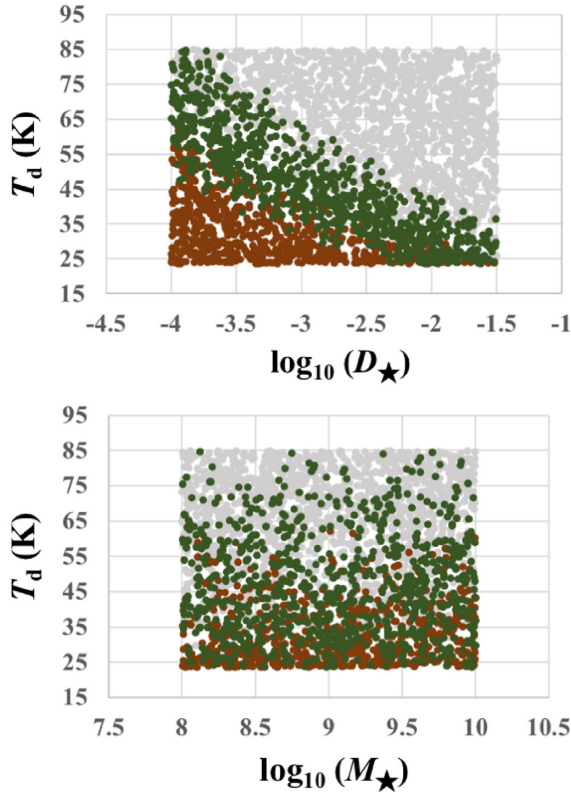
---

[1] https://almascience.nao.ac.jp/proposing/sensitivity-calculator

Figure 1. Effects of the selection criterion IRX < $\mathrm{IRX}_{\mathrm{max}}$ in the basic parameter space ($M_\star$, $\mathcal{D}_\star$, T_d). The data points in the 3D space are projected on to the T_d–$\mathcal{D}_\star$ (upper) and T_d–$M_\star$ planes (lower). The data points in colour are selected with $\mathrm{IRX}_{\mathrm{max}} = 10$, while those in brown are with $\mathrm{IRX}_{\mathrm{max}} = 1$; that is, the green points indicate objects with $1 \le \mathrm{IRX} < 10$. The grey points show the data with $\mathrm{IRX} \ge 10$; thus, they are not used in the analysis in this paper.

We hereafter adopt $\mathrm{IRX}_{\mathrm{max}} = 10$. Thus, galaxies with $\mathrm{IRX} > 10$ shown in grey in Fig. 1 are removed from the sample. In the end, we have 1 510 objects with $\mathrm{IRX} \le 10$. If we adopt $\mathrm{IRX}_{\mathrm{max}} = 1$, the number of high-$T_\mathrm{d}$ objects decreases. There are some observational clues to the maximum value of IRX at $z > 5$. Fudamoto et al. (2020) using stacked data showed that the IRX is typically smaller than 1 at $z = 5.5$ in the stellar mass range we consider. However, the stacked data do not constrain the maximum IRX. They also showed detected data points around $M_\star \sim 10^{10}\,\mathrm{M}_\odot$ with $\log \mathrm{IRX} \sim 0.5$, implying the existence of objects with $\mathrm{IRX} > 1$. Hashimoto et al. (2019)[2] estimated that some LBGs at $z \gtrsim 7$ have $\mathrm{IRX} = 1$–10. Since ALMA-detected LBGs are rare at $z > 5$, simulations also help to derive expected ranges of IRX: Ma et al. (2019) showed that IRX extends up to 10 at $M_\star \gtrsim 10^9\,\mathrm{M}_\odot$ (see also Vijayan et al. 2021). However, $\mathrm{IRX} \lesssim 1$ at $M_\star < 10^9\,\mathrm{M}_\odot$. Thus, applying $\mathrm{IRX}_{\mathrm{max}} = 10$ could overestimate the detectability of objects with $M_\star$ less than $10^9\,\mathrm{M}_\odot$. However, we show below that such low-$M_\star$ LBGs are hardly detected even with $\mathrm{IRX}_{\mathrm{max}} = 10$. Thus, the possibility of lower IRX for low-$M_\star$ LBGs does not affect our conclusions. We still mention the results with $\mathrm{IRX}_{\mathrm{max}} = 1$ in Section 3.3.3, but we focus on the calculations of $\mathrm{IRX}_{\mathrm{max}} = 10$ unless otherwise stated.

[2]Some papers define $\log \mathrm{IRX}$ as IRX.

3.2 Characteristics of detected objects

Now we examine the detectability by ALMA for the selected sample. We particularly examine in which sense the detected objects are biased in terms of the dust temperature.

3.2.1 T_d versus L_{IR}

First, we focus on the two quantities related to dust emission: T_d and L_{IR}. In Fig. 2, we show the distribution of the sample on the T_d–L_{IR} diagram. Since the detectability depends on the observational band and the redshift, we separately plot nine panels for $\lambda = 450$, 850, and 1200 μm (ALMA Bands 9, 7, and 6, respectively) and $z = 5$, 7, and 10. Note that the distribution of the data points is almost the same for all the panels, and the only difference among various redshifts is caused by the lower bound of the dust temperature constrained by the CMB temperature. Since the SED is determined by T_d and L_{IR}, it is possible to calculate the detection limit analytically as shown by the solid yellow curves. As expected, the detected objects have larger L_{IR}. The number of detectable objects at 450 μm is significantly smaller than those at the other wavelengths. Moreover, at $z = 10$, the wavelength where the SED peaks shifts beyond 450 μm (i.e. 450 μm is located on Wien's side) so that the detection becomes significantly difficult. In contrast, the detection at 850 and 1200 μm is not sensitive to the redshift because of the so-called negative K correction. The difference in the number of detected objects at 850 and 1200 μm is only 10 per cent. All the objects detectable at 450 μm can be detected at 850 and 1200 μm.

We also observe that the detection is sensitive to the dust temperature at 850 and 1200 μm while it is less so at 450 μm. With the same L_{IR}, lower-T_d objects are more easily detected at 850 and 1200 μm: Objects with $L_{\mathrm{IR}} \sim$ a few $\times\,10^{10}\,\mathrm{L}_\odot$ can be detected if $T_\mathrm{d} \lesssim 30$ K, and only very IR luminous objects with $L_{\mathrm{IR}} \gtrsim 10^{11}\,\mathrm{L}_\odot$ can be detected if $T_\mathrm{d} \gtrsim 45$ K. With a fixed total IR luminosity, the SED peak shifts towards a longer wavelength for lower T_d, so that the detection at wavelengths 850 and 1200 μm, which are mostly located on the Rayleigh–Jeans side, becomes easier. This is the reason why the detected objects at 850 and 1200 μm are biased towards low dust temperature (e.g. Chapman et al. 2005), as further discussed in Section 3.3. In contrast, the boundary of the detected objects (yellow solid line) is less inclined in the 450 μm band, since it is located around the SED peak at $z \sim 5$–7. Thus, the change of dust temperature has a smaller influence on the detectability in the 450 μm band than in the longer-wavelength bands. As shown later, the 450 μm band is not bias-free, but the 450 μm sample covers the entire range of dust temperature. Moreover, all objects detected at 450 μm are detected at 850 and 1200 μm. Therefore, a survey at such a short wavelength as 450 μm is useful to construct a (sub)sample, whose dust temperature is known. In this sense, a survey data at 450 μm would be useful to overcome the dust temperature bias at $z \sim$ 5–7. The sample size is yet limited by the shallowness of the 450 μm observations. This means that a deeper survey at 450 μm is crucial to further increase the size of the sample whose dust temperature is known. We discuss a possibility of a deeper survey in Section 4.2.

3.2.2 T_d versus $M_\star$ (L_{UV})

Next, we show the T_d–$M_\star$ relations in Fig. 3. We observe that there is a tendency that objects with larger $M_\star$ are more easily detected. However, a high stellar mass does not necessarily lead to detection. This is because of the difference in the dust abundance ($\mathcal{D}_\star$; see Section 3.1). As mentioned above, the detection at 450 μm
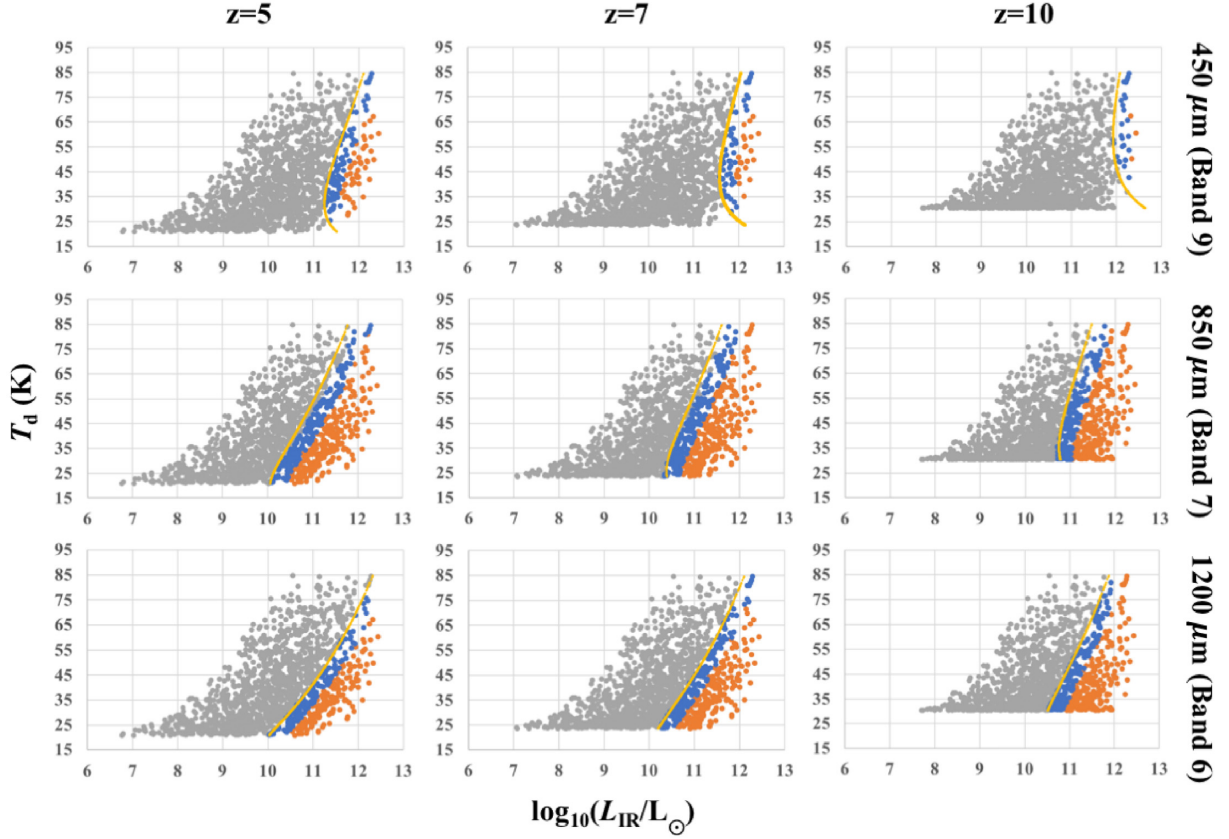
Figure 2. T_d versus L_{IR} for the three different redshifts, $z = 5$, 7, and 10 at 450, 850, and 1200 μm (ALMA Bands 9, 7, and 6, respectively) as indicated on the top and on the right side. Only objects with IRX ≤ 10 are plotted. The orange and blue points represent galaxies which can be detected (3σ) with integration time <1 h and 1–5 h with ALMA, respectively. The grey points indicate objects not detected with 5 h of integration. The yellow solid line is the analytically calculated detection limit corresponding to the ALMA 5-h integration (3σ).

is extremely hard at $z = 10$. For $z = 5$ and 7, detected galaxies at 450 μm have $\log(M_\star/M_\odot) \gtrsim 9.5$, while objects with a wider variety in $M_\star$ ($\gtrsim 10^{8.5}$ M$_\odot$) are detected at 850 and 1200 μm. This difference reflects the different depths. At 450 μm, although there is a tendency that galaxies with high $M_\star$ are more easily detected, there is not a clear trend that higher- or lower-T_d objects are more easily detected for a fixed $M_\star$ at $T_d \gtrsim 30$ K. At 850 and 1200 μm, lower-T_d objects ($T_d \lesssim 40$ K) are more easily detected at low $M_\star \sim 10^9$ M$_\odot$ (further discussed in Section 3.3). For the difference in the detectability among the redshifts and bands, see Section 3.2.1.

3.3 Detection probability

In the above, we adopted two reference quantities: L_{IR} and $M_\star$. The detectability for various T_d is different depending on which of these two quantities is used for the sample selection. We show the detectability as a function of T_d using one of the above two quantities (L_{IR} and $M_\star$) as a reference. If we use L_{IR} and $M_\star$ for the reference quantity, we, respectively, refer to the sample as *the IR-referenced sample* and *the UV-referenced sample* (recalling that $M_\star$ is originally derived from the UV luminosity by assumption).

Here, we show the detection probability, which is defined as the fraction of the detectable objects to the generated sample in each of the bins set below. The above sample size is still small to show the statistical properties for various bins of dust temperature, stellar mass, and IR luminosity. Thus, for the purpose of showing the detection probability, we boost the sample by 10 times with the same procedure

as described in Section 2.3. We adopt the 5-h detection limit (3σ) for ALMA. The objects are divided into six bins for the dust temperature with 10 K difference from 25 to 85 K. We also divide $\log L_{IR}$ into three bins with a bin size of 0.5 dex in $\log(L_{IR}/L_\odot) \geq 11$, and $M_\star$ into four bins with a bin size of 0.5 dex in $\log(M_\star/M_\odot) = 8$–10. Since no objects can be detected at 450 μm at $z = 10$, we only show the results at $z = 5$ and 7.

3.3.1 IR-referenced sample

We show the resulting detection probability for various ranges of L_{IR} in Fig. 4. The detection probabilities are shown separately for $\log(L_{IR}/L_\odot) = 10.5$–11, 11–11.5 and >11.5; note that we only show $\log(L_{IR}/L_\odot) > 11$ for 450 μm at $z = 5$ and $\log(L_{IR}/L_\odot) > 11.5$ for 450 μm at $z = 7$ because less luminous galaxies are not detected. If the IR luminosity is high, the detection probability is high as expected. However, even for $\log(L_{IR}/L_\odot) > 11$, the detection is strongly biased towards lower T_d at all wavelengths at both $z = 5$ and 7. In particular, the bias is sharp at 850 and 1200 μm in the sense that almost all objects are detected at low T_d, while almost none is detected at high T_d. The dust temperature at which this transition from detection to non-detection occurs depends on L_{IR} with higher L_{IR} allowing detection up to higher dust temperature. At 450 μm, the decline of the detection probability towards higher T_d is milder, although the sensitivity is less than the other bands. This is consistent with the discussion in Section 3.2.1. Although the 450 μm sample is useful to determine the dust temperature, the sample size is made small by
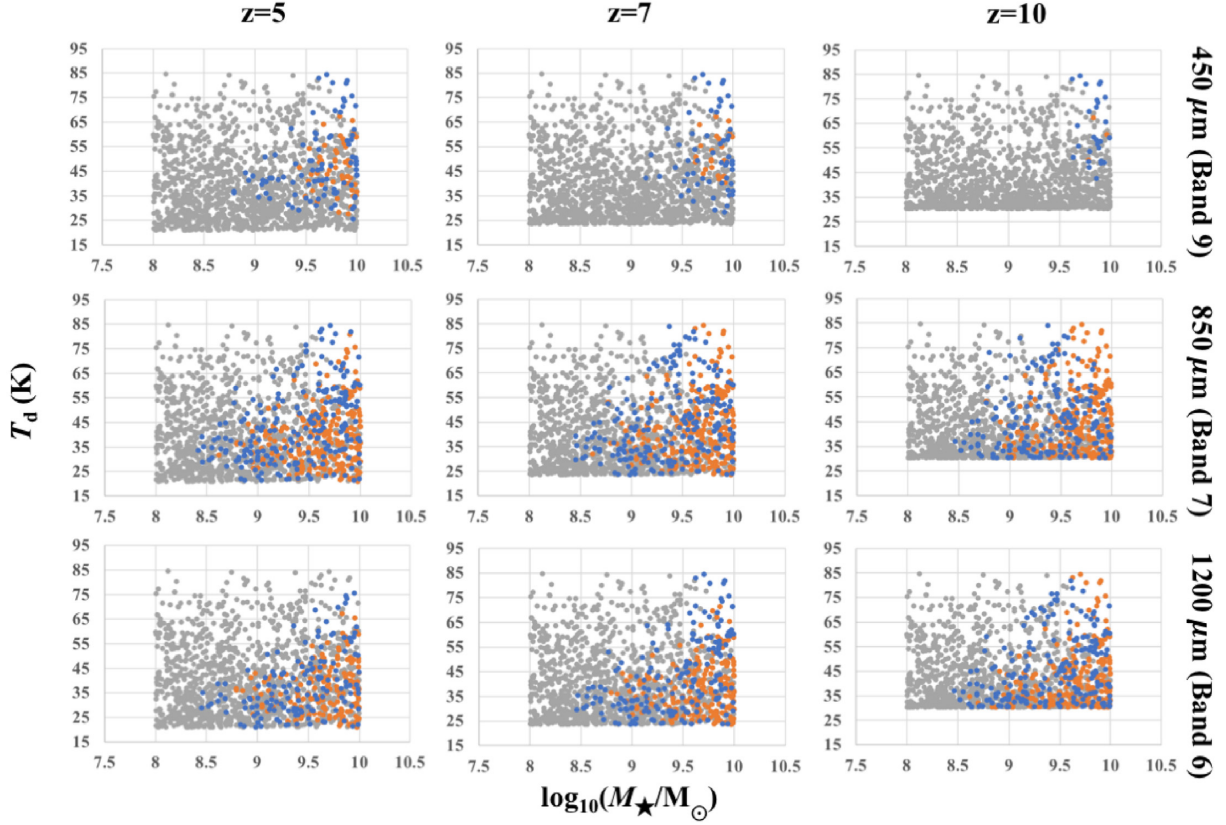
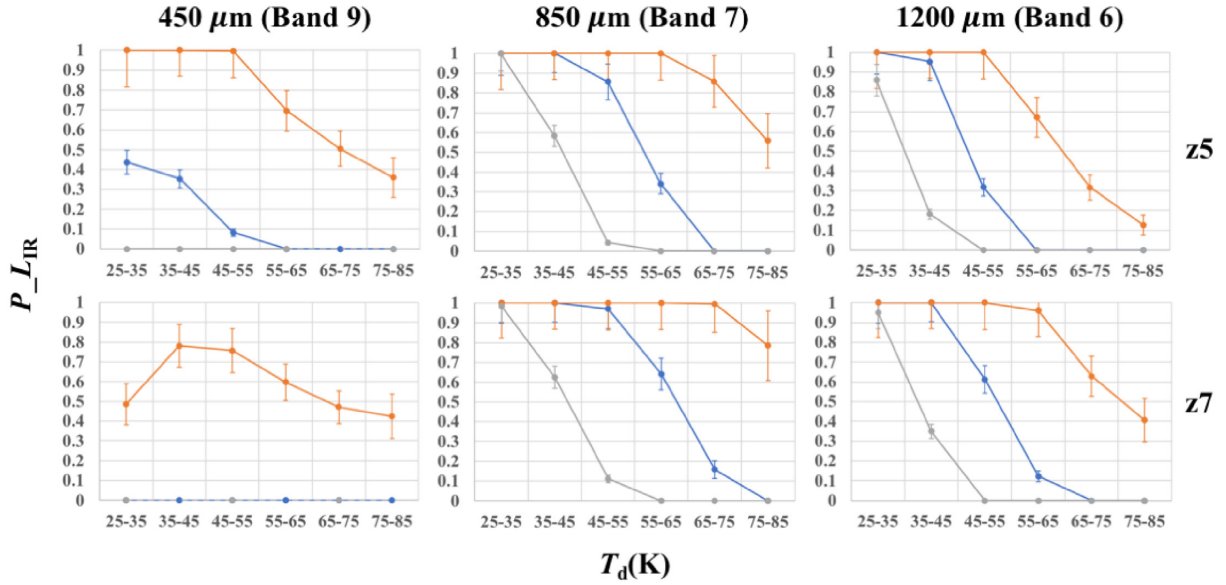**Figure 3.** Same as Fig. 2 but showing the T_d–$M_\star$ diagrams.

Figure 4. Detection probability as a function of dust temperature (binned with 10 K width) for various ranges of L_{IR}. The left-hand, middle, and right-hand panels show the results in the 450, 850, and 1200 μm bands (ALMA Bands 9, 7, and 6), respectively, and the upper and lower panels present $z = 5$ and 7, respectively. The grey, blue, and orange lines represents the sample with conditions $10.5 < \log(L_{IR}/L_\odot) < 11$, $11 < \log(L_{IR}/L_\odot) < 11.5$ and $11.5 < \log(L_{IR}/L_\odot)$, respectively. Note that objects with $\log(L_{IR}/L_\odot) < 11$ (<11.5) are not detected in the 450 μm band at $z = 5$ (7).
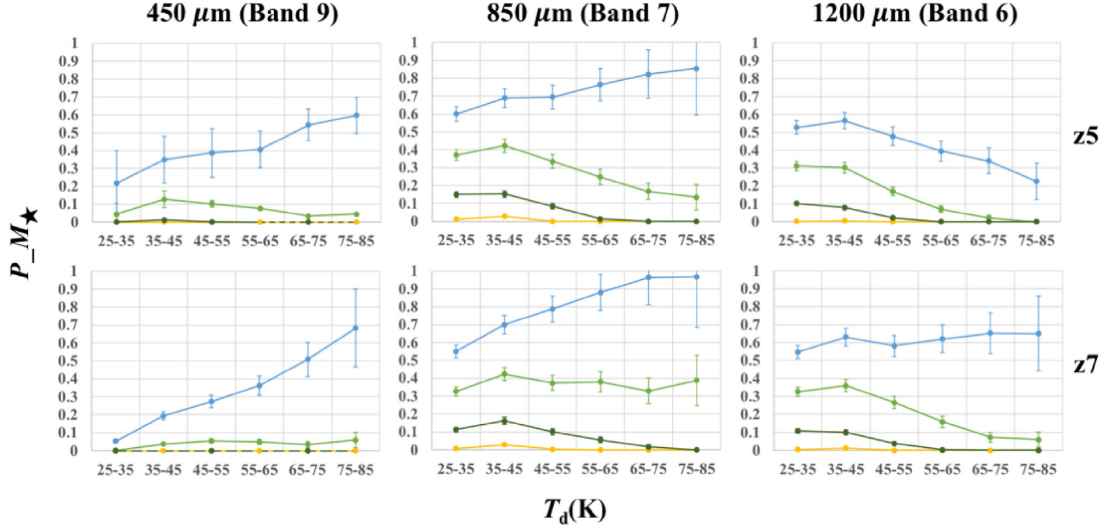The bars show the Poisson errors.

Figure 5. Same as Fig. 4 but based on the UV ($M_\star$) selection. The yellow, dark green, light green, and blue lines represent the sample with conditions $8 < \log(M_\star/M_\odot) < 8.5$, $8.5 < \log(M_\star/M_\odot) < 9$, $9 < \log(M_\star/M_\odot) < 9.5$, and $9.5 < \log(M_\star/M_\odot) < 10$, respectively. Note that objects with $\log(M_\star/M_\odot) < 9$ are not detected in the 450 μm band at $z = 7$.

requiring the detection at 450 μm. Deeper 450 μm surveys in the future will be useful as we discuss further in Section 4.2.

3.3.2 UV-referenced sample

We show the detection probability for various ranges of $M_\star$ in Fig. 5. The detection probabilities are shown separately for $\log(M_\star/M_\odot) = $ 8–8.5, 8.5–9, 9–9.5, and 9.5–10. Note that at 450 μm, only objects with $\log(M_\star/M_\odot) > 9$ (9.5) are detected at $z = 5$ (7). From Fig. 5, we observe that the temperature bias depends on the stellar mass. If the stellar mass is high, there is no significant dust temperature bias at 450 μm at $z = 5$ and 1200 μm at $z = 7$. There is a slight trend that higher-T_d objects are more easily detected in the 450 μm band at $z = 7$ while lower-T_d objects are more detectable at 1200 μm. At 850 μm, LBGs with $\log(M_\star/M_\odot) > 9.5$ are mostly detected with a slight bias towards high-T_d objects. Less UV-luminous objects with $\log(M_\star/M_\odot) < 9.5$ are biased towards low T_d for the 850 μm band in a similar way as observed for 1200 μm. These complex behaviours of the bias is due to the two completing effects: if the dust temperature is high, only low-dust-abundance objects are permitted as described in Section 3.1 (Fig. 1). Thus, more efficient dust emission with higher T_d competes with less dust with lower $\mathcal{D}_\star$.

The low detection rate of dust emission from LBGs at $z > 5$ by ALMA observations (e.g. Capak et al. 2015; Bouwens et al. 2016) is consistent with the low (half or less) detection probabilities in Band 6 (1200 μm; Fig. 5 right), which is often used to observe dust emission at high redshift. More quantitatively, in a recent sample from Schouws et al. (2021), who targeted LBGs at $z \gtrsim 7$ mostly with $\log M_\star/M_\odot \gtrsim 9.5$, 6 out of 15 LBGs are detected at ~1200 μm. The detection rate is ~40 per cent. Their integration time per object is roughly 1 h; if we use the detection limit for 1 h in our model, the detection probability becomes roughly half. Since our model predicts a detection rate of ~60 per cent at $z = 7$ in the 1200 μm band (Fig. 5), the above detection rate (40 per cent) is reasonable considering their shallower detection limit. Fudamoto et al. (2020) showed the detection rates in Band 7 as a function of stellar mass for galaxies at $z \sim 5$. Their on-source integration time is on average ~1/3 h. Thus, their detection limit is roughly four times higher

than that used above. In this case, the detected fraction is ~5 times smaller. Therefore, in the highest mass range ($M_\star = 10^{9.5}–10^{10}$ M$_\odot$), we predict a detection rate of ~10 per cent, which is consistent with their detection rate. In the range of $M_\star = 10^9–10^{9.5}$ M$_\odot$, the detection rate is predicted to be a few per cent, which is also consistent with their extremely low detection rate. Although our model needs further refinement for detailed comparison with observations, this broad success in explaining the detection rates supports our modelling in this paper.

For the current sample of $z > 5$ LBGs detected by ALMA, the stellar masses are broadly larger than $10^{9.5}$ M$_\odot$ (or the UV luminosity higher than $10^{10.7}$ L$_\odot$ from equation 6) and the detection is mostly based on Band 6 ($\lambda \sim 1200$ μm) or multiple bands including Band 6 (Willott et al. 2015; Faisst et al. 2020; Schouws et al. 2021). According to Fig. 5, the detection at $z = 5–7$ is not significantly biased or is slightly biased towards low T_d in Band 6. Thus, the high dust temperatures (40–70 K; Burgarella et al. 2020; see also the Introduction) obtained from the observations cannot be due to a bias but are reflecting the real trend.

3.3.3 Possible variations caused by α and IRX$_{max}$

Here, we discuss how much the variations of α and IRX$_{max}$, which could have a large diversity or uncertainty at high redshift (Section 2.2), affect the above detection probabilities.

As discussed in Section 2.2, a minor fraction of galaxies have large values of α ($\gtrsim 100$ L$_\odot$/M$_\odot$), which are out of the range we adopted. These very high values of α is predominantly due to extremely young ages (~10^7 yr). To examine the effect of large α on the detection probabilities, we examine a case where $\alpha = 100$ L$_\odot$/M$_\odot$ for all the generated sample. Since larger values of α mean larger L_{UV}, objects with larger L_{IR} are permitted under a fixed value of IRX$_{max}$. Thus, for the IR-referenced sample, the number of high-L_{IR} objects increases, but the detection probability at a fixed L_{IR} bin is not sensitive to the increase of α. In contrast, α directly affects the detection probabilities of the UV-referenced sample. The detection probabilities increase in any of the $M_\star$ bins broadly by a factor of ~2, but the trends among different dust temperatures and stellar masses are kept similar. Even

with this extreme value of α, the detection rate is less than 30 per cent for $M_\star < 10^9\,M_\odot$, for which large α is actually observed (Section 2.2). Considering that the large α only moderately affects the results, we argue that the discussions and conclusions in this paper are not much altered by the existence of objects with extremely large α.

For IRX, many LBGs may have lower values (~ 1) as mentioned in Section 3.1. Thus, we also examine a case of $IRX_{max} = 1$ instead of 10. We find that this case predicts completely suppressed detection of objects with $M_\star < 10^9\,M_\odot$, which are difficult to detect even with $IRX_{max} = 10$. The detection probability for $M_\star > 10^{9.5}\,M_\odot$ drops by half. For the IR-referenced sample, high-T_d ($T_d \gtrsim 60$ K) and high-L_{IR} ($L_{IR} \gtrsim 10^{11.5}\,L_\odot$) objects are eliminated because of the severer criterion for IRX. However, we regard $IRX_{max} = 1$ as an extreme assumption since some LBGs likely have $IRX > 1$ (Section 3.1).

4 DISCUSSION

4.1 Different grain species

Although we only showed the results for graphite, we also analysed different types of grains (AC and silicate; Table 1). The temperature biases in the IR-referenced and UV-referenced samples are similar to what we have shown using graphite. The detected number is ~ 26 (20) per cent larger for AC (silicate) than for graphite. Both AC and silicate slightly extend the sample towards higher dust temperatures (by at most 10 K) because the constraint from $IRX < IRX_{max}$ depends on C_{IR} and β_{IR} (equation 7). Moreover, a smaller β_{IR} for AC enhances the emission at long wavelengths, leading to more detected objects at 850 and 1200 μm. However, C_{IR} and β_{IR} do not modify the trend of the detection probability for T_d, so that the above conclusions are not qualitatively affected. We just note that the detection probability could be affected at most by a factor of 1.3 if we adopt other dust species than graphite.

4.2 Deeper 450 μm observations

In the above, the detected objects show different biases for T_d between 450 μm and 850 (or 1200) μm. However, the overall sample size is limited by the shallowness of the 450 μm band. The 450 μm band, which is near the SED peak or even on Wien's side of the SED, is also crucial to determine the dust temperature. A future large single-dish telescope in a site with a very low water vapour condition is expected to significantly improve the sensitivity at 450 μm (and in some shorter wavelength bands; nearly THz frequencies) compared with ALMA. The Antarctic Plateau provides the most suitable atmospheric condition for ground-based THz observations. Therefore, among various plans in the world, we focus on a 30 m THz telescope at New Dome Fuji (PI: Naomasa Nakai). We calculated the sensitivity using the following assumptions. We adopt the transmission achieved in 50 per cent of the time in winter; that is, 0.75 at 650 GHz (450 μm) obtained at Dome A. The transmission at New Dome Fuji is expected to be almost the same as that at Dome A (Yang et al. 2010). The precision of the antenna surface is 20 μm. For the sensitivity of the camera, we adopt $NEP = 6 \times 10^{-18}$ W Hz$^{-1/2}$. We obtain the expected detection limits (5σ) for a 10 h on-source integration at 450 μm as 0.069 mJy. One of the most important advantage of the 450 μm band compared with longer wavelengths is that the sensitivity is not confusion-limited because of a higher angular resolution. Therefore, large improvement of sensitivity at 450 μm is expected by future large single-dish telescopes if they are located in a site of good atmospheric condition.
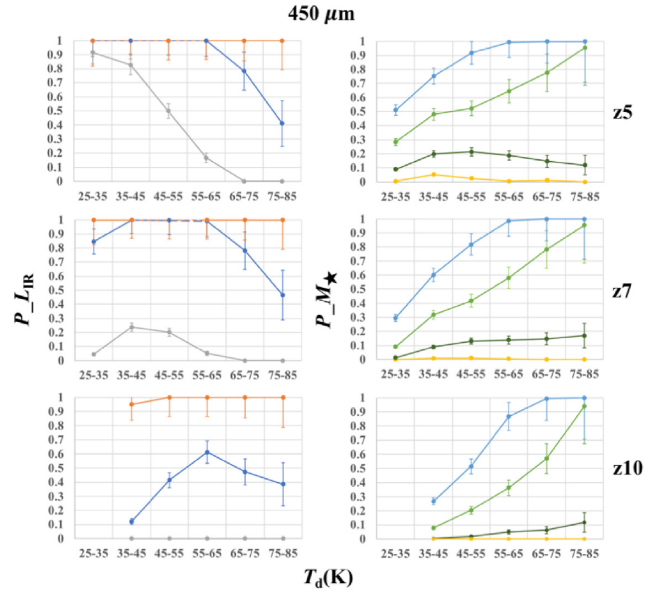

Figure 6. Detection probabilities for future sensitive 450 μm observations described in the text. The left and the right columns of panels are the same as Figs. 4 and 5, respectively, but only for 450 μm with the better sensitivity. Left: the grey, blue, and orange lines represents the sample with conditions $10.5 < \log(L_{IR}/L_\odot) < 11$, $11 < \log(L_{IR}/L_\odot) < 11.5$ and $11.5 < \log(L_{IR}/L_\odot)$, respectively. Right: the yellow, dark green, light green, and blue lines represent the sample with conditions $8 < \log(M_\star/M_\odot) < 8.5$, $8.5 < \log(M_\star/M_\odot) < 9$, $9 < \log(M_\star/M_\odot) < 9.5$ and $9.5 < \log(M_\star/M_\odot) < 10$, respectively. The upper, middle, and lower rows of panels show the results at $z = 5$, 7, and 10, respectively. At $z = 10$, we do not show the data in the temperature bin 25–35K because the CMB temperature lies in this range. Note that no LBG with $\log(L_{IR}/L_\odot) < 11$ is detected at $z = 10$ and none with $\log(M_\star/M_\odot) < 8.5$ and <9 is detected at $z = 7$ and 10, respectively.

We examine the same sample as in Section 3.3 but adopt the above deeper detection limit at 450 μm. The results for the IR- and UV-referenced samples are described in what follows.

4.2.1 IR-referenced sample

In Fig. 6 (left), we show the detection probability as a function of dust temperature for various ranges of L_{IR}. Compared with Fig. 4 (left), the detection probabilities rise significantly, especially for objects with $\log(L_{IR}/L_\odot) > 11$. Almost all LBGs with $\log(L_{IR}/L_\odot) > 11.5$ are detected at both $z = 5$ and 7, and even objects with $11 < \log(L_{IR}/L_\odot) < 11.5$ have twice higher detection probabilities than those by ALMA. Besides, some low-luminosity objects with $\log(L_{IR}/L_\odot) < 11$ can be detected. In summary, a nearly complete, IR-selected, sample can be constructed at $L_{IR} > 10^{11}\,L_\odot$ for high-redshift ($z = 5$–7) LBGs. As shown in Section 3.2.1, detection becomes difficult for $z = 10$ at 450 μm by ALMA. From Fig. 6, we observe for $z = 10$ that the detection probability for objects with $\log(L_{IR}/L_\odot) > 11.5$ is higher than 0.8 and that with $11 < \log(L_{IR}/L_\odot) < 11.5$ reaches almost half. Thus, we expect that more information for dust emission from LBGs at $z = 10$ can be obtained with the future telescope. At 850 and 1200 μm, ALMA is still preferable since a single-dish telescope survey becomes confusion-limited at such long wavelengths. Therefore, future 450 μm surveys with the 30 m class single-dish Antarctic telescope, combined with ALMA measurements at longer submm wavelengths, will be promising not

only to measure the dust temperature but also to construct a deeper IR-selected sample with little dust-temperature bias.

We also performed a calculation for 350 μm observations with the same future telescope but with a transmission of 0.71 (50 per cent in winter), and obtained detection probabilities similar to, but slightly worse than, the above 450 μm case. Thus, the 450 μm band is optimum for constructing an IR-selected LBG sample at $z = 5$–7. Note that optical observations will also be advanced in the future, so that the cross-identification with optical telescopes will not be a limiting factor to identify LBGs.

4.2.2 UV-referenced sample

As shown in Fig. 6 (right), objects with $\log(M_\star/M_\odot) > 9$ are biased towards high dust temperatures. This is interpreted as more efficient emission for higher dust temperatures. LBGs with lower $M_\star$ are not efficiently detected. The detection is improved compared with the ALMA 850 and 1200 μm bands for $9 < \log(M_\star/M_\odot) < 9.5$ (Fig. 5), particularly at high dust temperatures. Thus, the deep 450 μm observation is useful to detect high-T_d, intermediate-$M_\star$ objects, which tend to be missed by the current ALMA submm followup of LBGs. Some objects with $\log(M_\star/M_\odot) < 9$ are also detected. Therefore, in the future, we can obtain more information about low stellar mass objects, and the future 450 μm observations we considered here could be even deeper than the current ALMA 850 and 1200 μm observations in terms of the detected stellar mass range of LBGs.

5 CONCLUSION

We investigate if the current submm observations (represented by ALMA) are fairly tracing the dust temperature in high-redshift ($z \geq 5$) LBGs. To this goal, we perform a simple test using random realizations of LBGs with various stellar masses ($M_\star$), dust temperatures (T_d), and dust-to-stellar mass ratios ($\mathcal{D}_\star$). The values of these three quantities are chosen to cover the parameter space of observed LBGs at $z \geq 5$. We assume that the UV luminosity is strongly correlated with the stellar mass and that the stellar radiation is not highly obscured (IRX < 10).

We find that the dust temperature bias enters differently depending on the sample selection and the wavelength (in the observer's frame). If we consider a sample with a fixed range of the total IR dust luminosity L_{IR} (IR-referenced sample), the 850 and 1200 μm samples are biased to low dust temperatures ($\lesssim 45$ K) even if the IR luminosity is as high as $L_{IR} \gtrsim 10^{11}$ L$_\odot$. The 450 μm band is slightly less biased compared with the longer wavelengths, and is useful to determine the dust temperature; however, it is much shallower. If we select a sample (UV-referenced sample) with a fixed range of the UV luminosity (equivalent to $M_\star$ for LBGs in our model), the dust temperature bias is weaker compared with the IR-referenced sample. Note that the number of detectable LBGs decreases as the redshift becomes higher at 450 μm since the peak of dust emission SED shifts beyond 450 μm. In contrast, with the negative K correction, detection at 850 and 1200 μm is not sensitive to the redshift.

Although the dust temperature bias in a UV-referenced sample is milder than that in an IR-referenced one, there are still some biases, which depend on $M_\star$. There are competing effects between $\mathcal{D}_\star$ and T_d in determining the bias: Since we exclude high-IRX objects (not typical of LBGs), high-T_d objects tend to have low $\mathcal{D}_\star$. Thus, more efficient dust emission with a higher T_d can be counterbalanced by a lower dust abundance. Since the current ALMA detections of z

$\gtrsim 5$ LBGs predominantly sample LBGs with $M_\star > 10^{9.5}$ M$_\odot$ in the 1200 μm band, they should not be biased for high T_d according to our results. However, the detected LBGs have broadly high dust temperatures. Thus, the high T_d in high redshift LBGs reflects a real trend, not caused by a bias. We also find that the low detection rates of $z \gtrsim 5$ LGBs with ALMA are also consistent with our results.

The 450 μm band is differently biased for T_d from the 850 and 1200 μm bands, so that it can be useful to obtain an unbiased view of the dust temperature; however, it is much shallower than the longer-wavelength bands. Thus, we investigate a possibility of future deep 450 μm single-dish surveys. We particularly consider the future 30-m Antarctic THz telescope at New Dome Fuji, of which the low water vapour atmospheric condition improves the sensitivity at 450 μm. Applying the same model but a deeper detection limit, we show that it is possible to obtain an almost complete (i.e. without T_d bias) IR-selected sample in a luminosity range of $L_{IR} > 10^{11}$ L$_\odot$ at $z = 5$–7 LBGs and for $L_{IR} > 10^{11.5}$ L$_\odot$ at $z = 10$. A UV-referenced sample to be detected by this future telescope shows a bias towards high T_d, but the detection in the intermediate-$M_\star$ range [$9 < \log(M_\star/M_\odot) < 9.5$] is much improved compared with the ALMA 850 and 1200 μm bands, especially at high T_d. Thus, the deep 450 μm survey is useful to detect high-T_d, intermediate-$M_\star$ LBGs, which tend to be missed in the current submm follow-ups of LBGs. Besides, the future sensitive telescope is able to detect some LBGs with low IR luminosity [$\log(L_{IR}/L_\odot) < 11$] and low-stellar mass [$\log(M_\star/M_\odot) < 9$] at 450 μm. Therefore, to obtain an unbiased and deeper view of the first dust enrichment in the Universe, a future large single-dish telescope capable of observing at short submm wavelengths is useful.

DATA AVAILABILITY

Data related to this publication and its figures are available on request from the corresponding author.

REFERENCES

Aoyama S. et al., 2019, MNRAS, 484, 1852
Aoyama S., Hou K.-C., Hirashita H., Nagamine K., Shimizu I., 2018, MNRAS, 478, 4905
Bakx T. J. L. C. et al., 2020, MNRAS, 493, 4294
Bakx T. J. L. C. et al., 2021, MNRAS, 508, L58
Béthermin M. et al., 2015, A&A, 573, A113
Bianchi S., Schneider R., 2007, MNRAS, 378, 973
Boquien M., Burgarella D., Roehlly Y., Buat V., Ciesla L., Corre D., Inoue A. K., Salas H., 2019, A&A, 622, A103
Bouwens R. J. et al., 2016, ApJ, 833, 72
Buat V., Xu C., 1996, A&A, 306, 61
Burgarella D., Nanni A., Hirashita H., Theulé P., Inoue A. K., Takeuchi T. T., 2020, A&A, 637, A32
Calzetti D., Armus L., Bohlin R. C., Kinney A. L., Koornneef J., Storchi-Bergmann T., 2000, ApJ, 533, 682
Capak P. L. et al., 2015, Nature, 522, 455
Carroll S. M., Press W. H., Turner E. L., 1992, ARA&A, 30, 499
Casey C. M. et al., 2013, MNRAS, 436, 1919

Casey C. M. et al., 2018, ApJ, 862, 77

Cazaux S., Tielens A. G. G. M., 2004, ApJ, 604, 222

Chapman S. C., Blain A. W., Smail I., Ivison R. J., 2005, ApJ, 622, 772

Chen L.-H., Hirashita H., Hou K.-C., Aoyama S., Shimizu I., Nagamine K., 2018, MNRAS, 474, 1545

Dayal P., Ferrara A., 2018, Phys. Rep., 780, 1

Dayal P., Hirashita H., Ferrara A., 2010, MNRAS, 403, 620

Di Mascia F. et al., 2021, MNRAS, 503, 2349

Draine B. T. et al., 2007, ApJ, 663, 866

Dudzevičiūtė U. et al., 2021, MNRAS, 500, 942

Faisst A. L. et al., 2017, ApJ, 847, 21

Faisst A. L., Fudamoto Y., Oesch P. A., Scoville N., Riechers D. A., Pavesi R., Capak P., 2020, MNRAS, 498, 4192

Ferrara A., Hirashita H., Ouchi M., Fujimoto S., 2017, MNRAS, 471, 5018

Fudamoto Y. et al., 2020, A&A, 643, A4

Ginolfi M., Graziani L., Schneider R., Marassi S., Valiante R., Dell'Agli F., Ventura P., Hunt L. K., 2018, MNRAS, 473, 4538

Gjergo E., Granato G. L., Murante G., Ragone-Figueroa C., Tornatore L., Borgani S., 2018, MNRAS, 479, 2588

Gould R. J., Salpeter E. E., 1963, ApJ, 138, 393

Granato G. L. et al., 2021, MNRAS, 503, 511

Graziani L., Schneider R., Ginolfi M., Hunt L. K., Maio U., Glatzle M., Ciardi B., 2020, MNRAS, 494, 1071

Hashimoto T. et al., 2019, PASJ, 71, 71

Hirashita H. et al., 2016, PASJ, 68, R1

Hirashita H., Ferrara A., 2002, MNRAS, 337, 921

Hirashita H., Ferrara A., Dayal P., Ouchi M., 2014, MNRAS, 443, 1704

Hirashita H., Burgarella D., Bouwens R. J., 2017, MNRAS, 472, 4587

Hou K.-C., Aoyama S., Hirashita H., Nagamine K., Shimizu I., 2019, MNRAS, 485, 1727

Huang Y.-H., Hirashita H., Hsu Y.-H., Lin Y.-T., Nelson D., Cooper A. P., 2021, MNRAS, 501, 1336

Inoue A. K., Hirashita H., Kamaya H., 2000, PASJ, 52, 539

Inoue A. K., Hashimoto T., Chihara H., Koike C., 2020, MNRAS, 495, 1577

Kawabe R., Kohno K., Tamura Y., Takekoshi T., Oshima T., Ishii S., 2016, in Hall H. J., Gilmozzi R., Marshall H. K., eds, Proc. SPIE Conf. Ser. Vol. 9906, Ground-based and Airborne Telescopes VI. SPIE, Bellingham, p. 990626

Klaassen P. D. et al., 2020, in Marshall H. K., Spyromilio J., Usuda T., eds, Proc. SPIE Conf. Ser. Vol. 11445, Ground-based and Airborne Telescopes VIII. SPIE, Bellingham, p. 114452F

Knudsen K. K., Watson D., Frayer D., Christensen L., Gallazzi A., Michałowski M. J., Richard J., Zavala J., 2017, MNRAS, 466, 138

Laporte N. et al., 2017, ApJ, 837, L21

Larson R. B., 2005, MNRAS, 359, 211

Leśniewska A., Michałowski M. J., 2019, A&A, 624, L13

Liang L. et al., 2019, MNRAS, 489, 1397

Lim C.-F. et al., 2020, ApJ, 889, 80

Liu H.-M., Hirashita H., 2019, MNRAS, 490, 540

da Cunha E. et al., 2013, ApJ, 766, 13

da Cunha E., Charlot S., Elbaz D., 2008, MNRAS, 388, 1595

de Bennassuti M., Schneider R., Valiante R., Salvadori S., 2014, MNRAS, 445, 3039

Ma X. et al., 2019, MNRAS, 487, 1844

Magnelli B. et al., 2014, A&A, 561, A86

Mancini M., Schneider R., Graziani L., Valiante R., Dayal P., Maio U., Ciardi B., Hunt L. K., 2015, MNRAS, 451, L70

Mancini M., Schneider R., Graziani L., Valiante R., Dayal P., Maio U., Ciardi B., 2016, MNRAS, 462, 3130

Matsushita S. et al., 2017, PASP, 129, 025001

McKinnon R., Torrey P., Vogelsberger M., 2016, MNRAS, 457, 3775

McKinnon R., Torrey P., Vogelsberger M., Hayward C. C., Marinacci F., 2017, MNRAS, 468, 1505

Michałowski M. J. et al., 2017, MNRAS, 469, 492

Nanni A., Burgarella D., Theulé P., Côté B., Hirashita H., 2020, A&A, 641, A168

Nozawa T., Kozasa T., Umeda H., Maeda K., Nomoto K., 2003, ApJ, 598, 785

Nozawa T., Kozasa T., Habe A., Dwek E., Umeda H., Tominaga N., Maeda K., Nomoto K., 2007, ApJ, 666, 955

Omukai K., Tsuribe T., Schneider R., Ferrara A., 2005, ApJ, 626, 627

Popping G., Somerville R. S., Galametz M., 2017, MNRAS, 471, 3152

Pozzi F. et al., 2021, A&A, 653, A84

Riechers D. A. et al., 2014, ApJ, 796, 84

Riechers D. A. et al., 2020, ApJ, 895, 81

Schaerer D., Boone F., Zamojski M., Staguhn J., Dessauges-Zavadsky M., Finkelstein S., Combes F., 2015, A&A, 574, A19

Schneider R., Omukai K., Inoue A. K., Ferrara A., 2006, MNRAS, 369, 1437

Schouws S. et al., 2021, preprint (arXiv:2105.12133)

Schreiber C., Elbaz D., Pannella M., Ciesla L., Wang T., Franco M., 2018, A&A, 609, A30

Silva L., Granato G. L., Bressan A., Danese L., 1998, ApJ, 509, 103

Skibba R. A. et al., 2011, ApJ, 738, 89

Sommovigo L., Ferrara A., Pallottini A., Carniani S., Gallerani S., Decataldo D., 2020, MNRAS, 497, 956

Sommovigo L., Ferrara A., Carniani S., Zanella A., Pallottini A., Gallerani S., Vallini L., 2021, MNRAS, 503, 4878

Springel V., Hernquist L., 2003, MNRAS, 339, 289

Steidel C. C., Adelberger K. L., Giavalisco M., Dickinson M., Pettini M., 1999, ApJ, 519, 1

Takagi T., Vansevicius V., Arimoto N., 2003, PASJ, 55, 385

Takeuchi T. T., Ishii T. T., Nozawa T., Kozasa T., Hirashita H., 2005, MNRAS, 362, 592

Tamura Y. et al., 2019, ApJ, 874, 27

Tinsley B. M., 1980, Fund. Cosmic Phys., 5, 287

Todini P., Ferrara A., 2001, MNRAS, 325, 726

Valiante R., Schneider R., Salvadori S., Bianchi S., 2011, MNRAS, 416, 1916

Vijayan A. P. et al., 2021, preprint (arXiv:2108.00830)

Wang W.-H. et al., 2017b, ApJ, 850, 37

Wang W.-C., Hirashita H., Hou K.-C., 2017a, MNRAS, 465, 3475

Watson D., Christensen L., Knudsen K. K., Richard J., Gallazzi A., Michałowski M. J., 2015, Nature, 519, 327

Whitworth A. P., Boffin H. M. J., Francis N., 1998, MNRAS, 299, 554

Willott C. J., Carilli C. L., Wagg J., Wang R., 2015, ApJ, 807, 180

Yajima H., Shlosman I., Romano-Díaz E., Nagamine K., 2015, MNRAS, 451, 418

Yamasawa D., Habe A., Kozasa T., Nozawa T., Hirashita H., Umeda H., Nomoto K., 2011, ApJ, 735, 44

Yang H. et al., 2010, PASP, 122, 490

Zavala J. A. et al., 2021, ApJ, 909, 165

This paper has been typeset from a TEX/LATEX file prepared by the author.